Spatially Resolved Electrostatic Potential and Photocurrent Generation in Carbon Nanotube Array Devices

Michael Engel,[†,‡,#] Mathias Steiner,[§,#,*] Ravi S. Sundaram,[⊥,▽] Ralph Krupke,[†,‡,△] Alexander A. Green,[∥] Mark C. Hersam,[∥] and Phaedon Avouris[§]

[†]Institute of Nanotechnology, Karlsruhe Institute of Technology, 76021 Karlsruhe, Germany, [‡]DFG Center for Functional Nanostructures (CFN), 76028 Karlsruhe, Germany, [§]IBM Thomas J. Watson Research Center, Yorktown Heights, New York 10598, United States , [⊥]Max-Planck-Institute for Solid State Research, 70569 Stuttgart, Germany, [∥]Department of Materials Science and Engineering and Department of Chemistry, Northwestern University, Evanston, Illinois 60208, United States , and [△]Institut für Materialwissenschaft, Technische Universität Darmstadt, 64287 Darmstadt, Germany. [#]These authors contributed equally. [▽]Present address: Engineering Department, University of Cambridge, Cambridge CB3 0FA, United Kingdom.

ABSTRACT

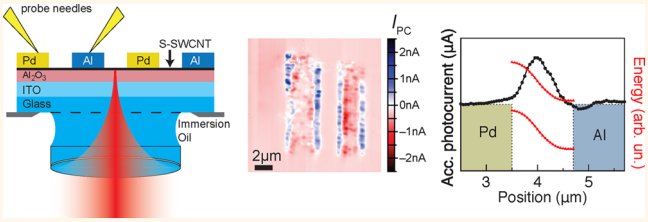

We have used laser-excited photocurrent microscopy to map the internal electrostatic potential profile of semiconducting single-walled carbon nanotube (S-SWCNT) array devices with a spatial resolution of 250 nm. The measurements of S-SWCNTs on optically transparent samples provide new insights into the physical principles of device operation and reveal performance-limiting local heterogeneities in the electrostatic potential profile not observable with other imaging techniques. The experiments deliver photocurrent images from the *underside* of the S-SWCNT−metal contacts and thus enable the direct measurement of the charge carrier transfer lengths at the palladium−S-SWCNT and aluminum−S-SWCNT interfaces. We use the experimental results to formulate design rules for optimized layouts of S-SWCNT-based photovoltaic devices. Furthermore, we demonstrate the external control of the electrostatic potential profile in S-SWCNT array devices equipped with local metal gates.

KEYWORDS: nanoelectronics · nano-optics · self-assembly

Semiconducting carbon nanotubes (S-SWCNTs) are a promising material for electronic and optoelectronic applications.[1] In electronics, S-SWCNTs are explored as a potential channel material for field-effect transistors.[2] Within an optoelectronic device, S-SWCNTs could take up various functionalities and perform as light-absorbing and -emitting layers,[3−9] as the electrically conducting channel,[10] and as (transparent) electrodes.[11] Several studies have been carried out with devices made of individual S-SWCNTs,[4,12−14] revealing that the total drive currents and photocurrents achieved are much lower than in conventional devices made of bulk semiconductors. It is hence necessary to increase the number of S-SWCNTs in a device in order to scale the electrical current level and the light-sensitive device area.[15,16] The electronic performance of a S-SWCNT array is largely determined by the physics of S-SWCNT−metal contacts,[17,18] as is the case with devices made of an individual S-SWCNT.[19,20] The electrostatic potential configuration at S-SWCNT−metal contacts determines the charge carrier transmission efficiency[18] and is mainly responsible for the photovoltaic response observed.[5] However, previous optical studies on S-SWCNT devices have been restricted to the device channel.[5,21] In order to be able to study S-SWCNT−metal contacts and the internal potential profile of S-SWCNT devices with high spatial resolution, it is beneficial to use a transparent device that enables its full optical inspection.

In this article, we investigate optically transparent S-SWCNT array devices in which S-SWCNTs act as the light-absorbing layer and simultaneously promote the carrier separation and transport to metallic electrodes. Upon illumination a photon is absorbed into a higher excited state of a S-SWCNT followed by a formation of a bound electron−hole pair (exciton) and a separation of the exciton into free carriers at opposite metallic contacts by an internal electric field; see ref 1 and references therein. The efficiency of the conversion is largely determined by the strength of the internal electric field but also depends on the nature of the S-SWCNT involved, the dielectric environment of the S-SWCNT, and specifics of the

* Address correspondence to msteine@us.ibm.com.

Received for review May 31, 2012 and accepted July 6, 2012.

Published online July 07, 2012
10.1021/nn302416e

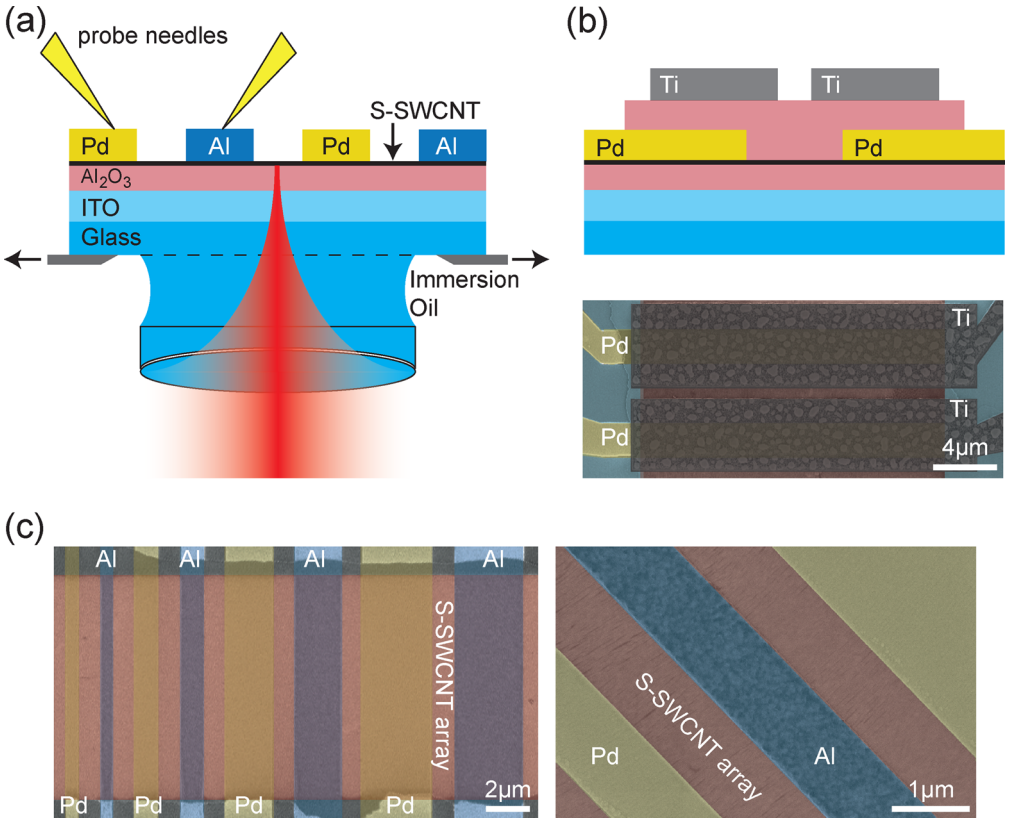

Figure 1. (a) Schematic of a S-SWCNT device built on an optically transparent multilayer substrate for studying photocurrent generation from the underside with an inverted scanning optical microscope. (b) Device schematic of a S-SWCNT array photodiode based on split top gates and colorized scanning electron microscope image of such a device (yellow: Pd electrodes, green: Ti split gates, and red: S-SWCNT array). (c) Colorized scanning electron microscope images of a S-SWCNT array device with alternating contacts as schematically indicated in (a) (yellow: Pd electrodes, blue: Al electrodes, and red: S-SWCNT array). The density in the array is about 50S-SWCNT/μm.

S-SWCNT–metal contacts. The external quantum efficiency of the process is on the order of 10^{-2} electrons per incident photon.[1] The dependence of the photocurrent on the internal field distribution is the basis for mapping the internal electrostatic potential profile of S-SWCNT array devices.

We have implemented and investigated two different device concepts: (1) Metal–S-SWCNT–metal junctions in which a built-in electric field across the S-SWCNT array is achieved by using two different contact metals. The work function difference of the metals creates a built-in electric field across the S-SWCNT array with an electrostatic potential gradient that separates electron–hole pairs (excitons) into free carriers at opposite contacts.[22,23] (2) S-SWCNT array p–i–n junction devices with split top gates made of metal. In this case, we use electrostatic field doping through the local gates in order to create a potential drop across the S-SWCNT array, as has been demonstrated previously for single S-SWCNTs[12,24,25] and S-SWCNT arrays.[26]

The S-SWCNTs used in this study are highly separated (>99% semiconductor purity) by density gradient ultracentrifugation[27,28] and self-assembled from solution by an evaporation-driven process[16] to form aligned arrays on a thin glass substrate. They have an average diameter of 1.5 nm, which corresponds to a band gap of ΔE = 0.7 eV.[29] The optically transparent substrate allows us to perform high-resolution, immersion-assisted photocurrent microscopy in functioning devices. In general, photovoltaic devices are compared by means of their external quantum efficiency, their open-circuit voltage, and their short-circuit current density that characterize the device performance when globally illuminated.[30] For S-SWCNT array devices with their high degree of heterogeneity, however, it is necessary to investigate the internal electrostatics with spatial resolution in order to test the fundamentals of device operation and to reveal the causes of performance limitations. High-resolution photocurrent microscopy allows us to map the internal potential profile of S-SWCNT array devices, revealing local potential heterogeneities that affect the performance of the S-SWCNT array device as a whole. Moreover, they allow us to monitor how electrostatic doping controls the local potential profile and photocurrent generation in a S-SWCNT array device.

RESULTS

Figure 1a shows the experimental setup and sample design. We use an inverted optical microscope in

combination with a multiaxis scanning stage for raster scanning the sample with respect to a tightly focused laser beam with nanometer precision. By using immersion oil in combination with a microscope objective having a high numerical aperture (NA = 1.25), we achieve a small optical excitation volume. The sample mount is equipped with electrical probes that are used for connecting devices with the electronic measurement system. For photocurrent measurements, we convert the short-circuit photocurrent between the source and drain (ground) electrodes into a voltage signal by using a current preamplifier and a source meter that are synchronized with a controlling computer and the optical scanning system. Control of bias conditions and electronic transport measurements are accomplished by the same system. The optical excitation/detection path from the underside of the sample requires an optically transparent, dielectric substrate with the functionality of a multiterminal electronic device. As a device platform, we use commercially available glass substrates coated with ITO that allow application of e-beam lithography and standard micro/nanofabrication techniques (see Methods section).[31]

S-SWCNTs are assembled from solution by the evaporation-driven method reported in ref 16, forming dense and highly aligned arrays on the optically transparent substrate. Figure 1b schematically shows a S-SWCNT array device having split top gates made of metal. By applying appropriate voltages to each of the two split gate electrodes it is possible to generate p- and n-doped spatial domains underneath the electrodes and, ultimately, to create an electrostatic potential drop within the S-SWCNT array. An alternative approach for making a S-SWCNT array junction device is depicted in Figure 1c. In this case, the operation principle is based on the energy band alignment at the S-SWCNT−metal contacts. The work function difference $\Delta\phi$ of the contact metals causes a built-in electric field near the interfaces of the device without the need for applying an external bias.[22] In the present case, we use aluminum and palladium as contact metals to induce the built-in electric field across the S-SWCNT array. The Fermi level of aluminum aligns closer to the conduction band of S-SWCNTs, while that of palladium aligns with the valence band of S-SWCNTs.[19,32] The metal work function difference is $\Delta\phi = \phi_{Pd} - \phi_{Al} \approx 1$ eV,[32] and the Schottky barriers at the S-SWCNT−metal contacts are relatively small, around $\Delta E = 20$ meV for S-SWCNTs with a diameter of 1.5 nm.[22,32] We hence expect a built-in electric field along the device channel (S-SWCNT array) that is proportional to the work function difference $\Delta\phi$ of the contact metals and inversely proportional to the channel length L_C. This potential can be further augmented by a thermovoltage contribution resulting from laser-induced heating.[33]

Figure 2a,b show optical microscopy images of such a device having alternating contacts made of Al and Pd, respectively, positioned along an aligned S-SWCNT array as shown in Figure 1c. The images were taken by raster scanning a $15 \times 15\ \mu m^2$ device area with a step size of 50 nm with respect to a tightly focused laser beam having a wavelength of $\lambda_{Laser} = 632.8$ nm. The polarization of the laser is adjusted parallel to the long axis of the S-SWCNTs in the array (*i.e.*, perpendicular to the orientation of the metal contacts). By using the oil immersion, the elastic scattering images and the photocurrent images of the same device area reveal higher contrast and improved optical resolution is obtained. The somewhat larger spatial extension of photocurrent features in the *x*-direction is a result of the horizontal alignment of the S-SWCNTs in the array, perpendicular to the contacts (see Figure 1c). The optical resolution of the short-circuit photocurrent images is determined on the basis of the vertical cross sections along two positions for each experimental condition (indicated by arrows in Figure 2a,b).

We quantify the spatial resolution of the photocurrent measurements by fitting features taken from the photocurrent cross sections with a Gaussian function and extract the full-width-at-half-maximum (fwhm) feature size. We obtain a spatial resolution of $\Delta_{im} = 250 \pm 40$ nm as compared to $\Delta_{air} = 500 \pm 60$ nm for the same feature if measured without oil immersion. On the basis of the density of 50 S-SWCNTs/micrometer derived from the electron microscopy images, we conclude that on average about 15 S-SWCNTs are simultaneously illuminated by the focused laser, and we estimate a responsivity of 0.01 nA/μW per S-SWCNT in the array. Hence, the features observed in the photocurrent images cannot be attributed to individual S-SWCNTs. However, the heterogeneous electrostatic potential profile seen in Figure 2b is not expected on the basis of the structure of the S-SWCNT array imaged by higher resolution SEM in Figure 1c. The internal, local potential heterogeneities affect the overall device performance and cannot be observed with optical techniques based on global illumination schemes. We note that the responsivity value given above provides a useful measure for the comparison of different nanotube device concepts or for the comparison with devices made of other low-dimensional materials. The comparability with conventional photodetectors is however limited because the detection volumes provided by a 3D semiconductor are much larger than those provided by a quasi 2D array of carbon nanotubes. Embedding a carbon nanotube array in an optical microcavity[34] could be a means to improve the responsivity. While carbon nanotube array devices are not yet competitive within the performance metrics of standard semiconductor devices, they offer unique opportunities for cost-efficient production of novel technologies such as flexible, all-organic optoelectronics.[35]

In order to correlate the spatially resolved photocurrent with the internal potential profile of the device, we accumulate the photocurrent data shown in

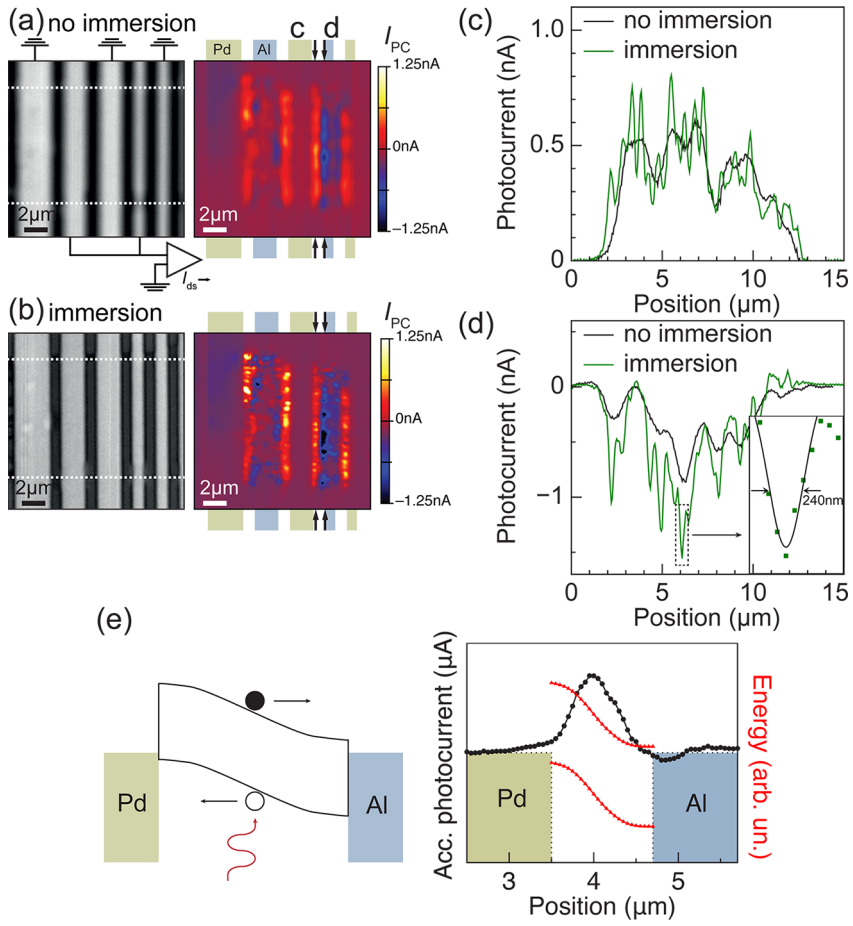

Figure 2. (a, b) Laser scanning microscope images (λ_{Laser} = 632.8 nm) of the device depicted in Figure 1c that were taken by recording the elastically scattered laser light (left) and the short-circuit photocurrent (right). The measurements shown in (a) were performed without immersion oil; the ones in (b) were performed with immersion oil. The circuitry for measuring the photocurrent across multiple contact pairs is also indicated. (c, d) Comparison of the photocurrent amplitudes taken from vertical cross sections indicated by arrows in (a) and (b). (e) Left-hand panel: schematic energy band profile of the device and illustration of the charge carrier separation. Also indicated are the positions of the contact electrodes (yellow: Pd, blue: Al). Right-hand panel: plot of the photocurrent amplitude accumulated in the direction parallel to one contact pair based on the data shown in (b). The accumulated photocurrent is overlaid with the energy band profile that is obtained by numerically integrating the measured, accumulated photocurrent for two different offset energy values to allow for comparison with the schematic band profile. The location of the accumulated photocurrent maximum in the channel regime coincides with the position of the maximum gradient of the electrostatic potential profile.

Figure 2b along the vertical (*y*-) direction. In the right-hand panel of Figure 2e, we plot the accumulated photocurrent amplitude measured between a contact pair made of two different metals, *i.e.*, Pd and Al. The electrode position assignment in the photocurrent images is based on the elastic scattering images with a precision that is limited by the image pixel width (50 nm in the present case). As a first important observation, the maximum of the photocurrent amplitude is located in the channel regime between the two contacts. Charge carrier separation occurs within the entire channel, not only at the contacts, which is the case for efficient photodetection in devices with identical metal electrodes.[4,5,16] A band diagram that visualizes the physical principle of the photocurrent generation in a device made of two different work function metals is shown in the left-hand panel of Figure 2e. While the diode principle has been reported previously,[23] we provide the first experimental demonstration that photocurrent generation is indeed maximized near the channel center, not at the device contacts, for devices with contacts made of different metals. The measured short-circuit photocurrent is proportional to the local potential gradient, $I_{PC}(x) \propto -\mathrm{d}/\mathrm{d}x\ \phi(x)$, where x denotes the position along the device channel and $\phi(x)$ is the potential energy of the electronic band.[36,37] In order to determine the electrostatic potential profile based on the experimental data, we numerically integrate the measured photocurrent in the x-direction (*i.e.*, along the channel), and the result is shown in the right-hand panel of Figure 2e. The location of the photocurrent maximum coincides with the position of the maximum gradient of the electrostatic potential, in agreement with the schematic band diagram in the left-hand panel of Figure 2e.

We also observe a nonvanishing, positive photocurrent signal underneath the Pd contact and a negative

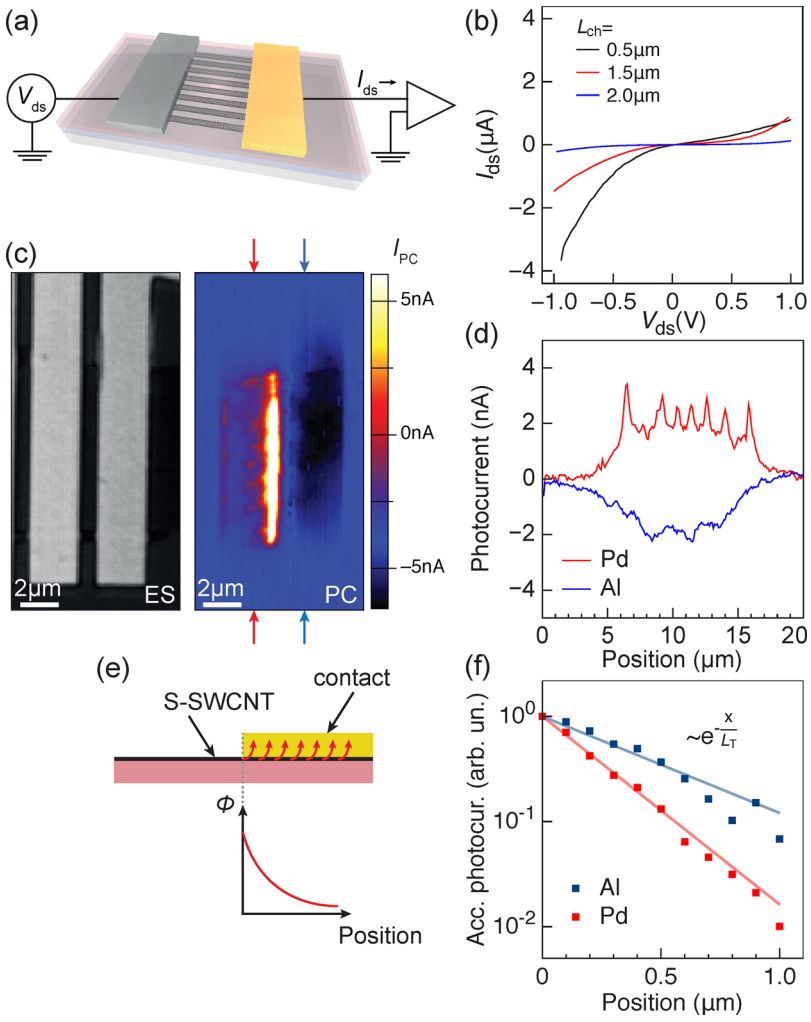

Figure 3. (a) 3D visualization of a Pd−S-SWCNT−Al array junction device. (b) Measured current−voltage characteristics of three devices having different channel lengths L_{ch}. (c) Microscope images showing elastic light scattering intensities (left) and short-circuit photocurrent amplitudes (right) measured on the same device. (d) Photocurrent amplitudes measured at the underside of the Pd−S-SWCNT contact (red) and the Al−S-SWCNT contact (blue) obtained from vertical cross sections of the image in (c) at the positions indicated by the blue and red arrows. (e) Schematics of charge carrier transfer and interface potential ϕ at the S-SWCNT−metal contact. (f) Semilog plot of the accumulated and normalized photocurrent amplitude measured at the underside of the Pd contact (red symbols) and Al contact (blue symbols). Exponential fits (lines) deliver the values of the characteristic charge carrier transfer length L_T at the respective S-SWCNT−metal interface.

one underneath the Al contact, as a result of the different interface potentials occurring at S-SWCNT-Pd and S-SWCNT-Al contacts, respectively. This experimental observation was not possible before because in previous studies[4,5] S-SWCNT−metal contacts were illuminated from the top. The photocurrent can be observed along the entire contact electrode width W if $W \leq 1\ \mu$m, indicating an incomplete carrier transmission at S-SWCNT−metal contacts with small widths. We note that for shorter W deviations from the ideal behavior displayed in Figure 2e can occur that lead to a shift of the spatial location of the photocurrent maximum or even a polarity inversion of the photocurrent amplitude.

On the basis of these observations we can deduce design rules for photovoltaic devices. In order to maximize the net photocurrent generated in a device that is fully exposed to light (globally illuminated), one should choose to maximize either positive or negative photocurrent contributions. In the present case, in order to maximize the net positive photocurrent across the multicontact device, one should reduce the channel length between adjacent contacts below the average S-SWCNT length, *i.e.*, $L_{ch} < L_{S\text{-}SWCNT}$. The measured width of the photocurrent maxima between the contacts is about 500 nm (fwhm), defining a lower limit of L_{ch}. As a result, the efficiency of photocurrent generation should increase, while the impact of undesired S-SWCNT−S-SWCNT percolation effects decreases. Furthermore, the measurement suggests contact widths of about $W_{Pd} < 1\ \mu m < W_{Al}$ in order to pin the location of maximum photocurrent generation in the channel center and to avoid incomplete carrier injection at the contacts. In the following, we investigate the

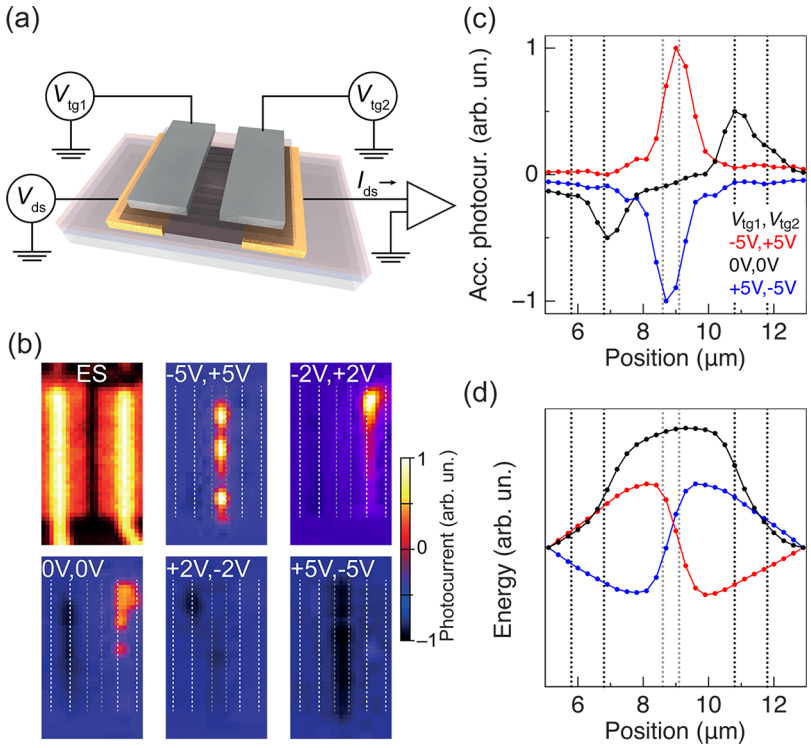

Figure 4. (a) 3D visualization of a S-SWCNT array device with symmetric contact metals and split top gates. (b) Top left shows the measured signal of elastically scattered light by a split gate device illuminated from the underside. The sequence of short-circuit photocurrent images was acquired for the different combinations of top gate voltages (V_{tg1}, V_{tg2}) as indicated; the image size is set to 7.5 × 13.5 μm^2. (c) Normalized accumulated photocurrent based on the data shown in (b) for (V_{tg1}, V_{tg2}) set to (−5 V, +5 V), (0 V, 0 V), and (+5 V, −5 V), respectively. Also indicated are the positions of the contacts and local gates. (d) Electrostatic potential profile obtained by numerical integration of the experimental, accumulated photocurrent amplitudes shown in (c).

specifics of charge carrier transfer at the different S-SWCNT−metal contacts.

Figure 3 shows a study of a Pd−S-SWCNT−Al device. Figure 3a schematically indicates the device layout and measurement scheme, while the measured current−voltage characteristics of three devices having different channel lengths are shown in Figure 3b. The transport measurements demonstrate that the degree of asymmetry of the electrical current is inversely proportional to the channel length L_{ch}, while a decrease of channel length L_{ch} increases the local built-in fields. By comparing the elastic laser scattering image of the device with the corresponding photocurrent image in Figure 3c, we can assign the position of the metal contacts. An important result is that the photocurrent amplitude does not vanish abruptly at the contact edges but clearly extends within the contacts, albeit having different polarities. In Figure 3d we compare cross sections taken from the photocurrent images measured underneath the Pd contact (along the red vertical line) and the Al contact (along the blue vertical line). Pronounced photocurrent features are visible in the cross sections that originate from single S-SWCNTs or small S-SWCNT bundles, as can be seen by following the photocurrent traces underneath the metal contacts in Figure 3c. In the following, we quantify the charge carrier transfer lengths based on the measured photocurrent amplitudes.

The decay of the photocurrent signal within the contact regime is expected to be exponential for a semiconductor/metal interface, and the characteristic decay length L_T of the contact potential $\phi(x) = \phi_0 \exp(-x/L_T)$ is referred to as the effective charge carrier transfer length.[18,38] The transfer length L_T characterizes the length scale of carrier transit between the S-SWCNTs and the metal contacts and determines the S-SWCNT−metal contact resistance R_C.[17] The measured photocurrent signal is proportional to the potential gradient, and we can write $I_{PC}(x) \propto -\,\mathrm{d}/\mathrm{d}x\,\phi(x) = -\tilde{\phi}_0 \exp(-x/L_T)$, which allows us to extract L_T values by fitting exponential model functions to the measured photocurrent amplitude. In Figure 3f we plot the fits of the normalized, accumulated photocurrent amplitude measured underneath the Pd (red) and Al (blue) contact. We obtain values of $L_T^{Pd} = 240 \pm 20$ nm for the Pd contact and $L_T^{Al} = 470 \pm 50$ nm for the Al contact. The L_T values constitute a lower bound for complete carrier transmission at the contacts. They are averaged over roughly 400 S-SWCNTs with an average diameter of $d = 1.5$ nm and are hence suited to represent the respective metal−S-SWCNT interface. We note that the L_T value of the S-SWCNT−Pd contact is in agreement with results from electrical transport measurements on single S-SWCNTs[39] and the L_T value of the Pd−graphene interface[40] while L_T values of S-SWCNT−Al contacts have not been previously reported.

Finally, we demonstrate the external control of the internal electrostatic potential profile of S-SWCNT array devices by means of local metal gates. A schematic of sample layout and bias scheme is shown in Figure 4a. In order to initially create a symmetric potential profile across the device, Pd was chosen as contact metal for both source and drain electrodes. Two split top gate electrodes define p- or n-doped spatial domains in the covered device areas through application of suitable voltage pairs (V_{tg1}, V_{tg2}). Figure 4b shows a series of short-circuit photocurrent images that were acquired for five different (V_{tg1}, V_{tg2}) combinations. Comparison with the elastically scattered optical signal allows for correlating the measured photocurrent signal with the positions of channel contacts and gate electrodes. Despite the Schottky barriers at the S-SWCNT−metal contacts, we do not expect any built-in fields in the device at zero gate bias. Indeed, for $V_{tg1} = V_{tg2} = 0$ V a small photocurrent response is observed only at the position of the contact edges.

In contrast, by applying either $V_{tg1} = -V_{tg2} = -5$ V or $V_{tg1} = -V_{tg2} = 5$ V, the maximum (minimum) photocurrent is observed in the intrinsic area of the S-SWCNT array framed by the p- and n-doped spatial domains, at the device center. Despite local heterogeneity that became obvious in the photocurrent images, the experimental data demonstrate that it is possible to control the spatial dependence of photocurrent generation in a S-SWCNT array by means of external electrostatic fields. In Figure 4c, we plot the normalized, accumulated photocurrent amplitudes for three representative gate voltage combinations (V_{tg1}, V_{tg2}), overlaid with the elastic scattering signal that indicates the position of contacts and gate electrodes. On the basis of the numerical integration of the accumulated photocurrent, we are able to reveal the electrostatic potential profile of the device (see Figure 4d). The initially flat and symmetric potential profile can be tuned such that a potential drop occurs in the region between the split gates with a slope that is determined by the local gate fields applied. As a result, the electrostatic potential in S-SWCNT arrays is well-defined by the applied gate fields. In Figure 4d we find that the intersection of the electrostatic potential profiles (red and blue line) is slightly shifted with respect to zero, the reference value at the contacts. The observation suggests that contributions of Schottky barriers at the contacts could offset the internal potential profile of the device.

CONCLUSION

We have studied the electrostatic potential and photocurrent generation in optically transparent S-SWCNT array devices by using laser-excited photocurrent microscopy with a spatial resolution of 250 nm, and we have imaged for the first time the underside of S-SWCNT−metal contacts in functioning optoelectronic devices. We have provided the first experimental evidence that the work function difference of Pd and Al as contact metals generates local built-in fields across a S-SWCNT array with maximum photocurrent generation efficiency near the channel center, not at the contacts, of the device. Moreover, we have directly measured a charge carrier transfer length of $L_T^{Pd} = 240 \pm 20$ nm at the S-SWCNT−Pd contact and of $L_T^{Al} = 470 \pm 50$ nm at the S-SWCNT−Al contact. On the basis of our experimental results, we have devised a strategy for improving the photovoltaic performance of multielectrode S-SWCNT array devices with contacts made of alternating metals. Furthermore, we have demonstrated external control of the location and the polarity of photocurrent in a S-SWCNT array by means of electrostatic field doping through local metal gates. Our results provide novel insights into S-SWCNT device physics and are important for the design and optimization of optoelectronic devices based on S-SWCNT arrays.

METHODS

We fabricate transparent S-SWCNT array devices based on commercially available microscope coverslips having a size of 20 × 20 mm^2 that are coated with ITO (SPI Supplies). The ITO has a sheet resistivity of 6−8 Ohm/sq. The purpose of the ITO layer is 2-fold. First, it can be utilized as a global back gate electrode, and second, it serves as a charge-dissipating layer, mitigating charging effects during e-beam lithography. In a first step we deposit 50 nm of Al_2O_3 by atomic layer deposition on top of the ITO layer. In the next step, we assemble S-SWCNT arrays on top of the Al_2O_3 *via* a self-assembly method reported in ref 16. In brief, the substrates are vertically immersed into highly purified (>99%) semiconducting S-SWCNT synthesized by the arc discharge method wrapped in SDS with a concentration of 0.1 mg/mL.[27,28] The S-SWCNT dispersion forms a pinning line on the sample surface that moves across the sample as the solvent evaporates, leaving behind areas with highly aligned S-SWCNT arrays. We then pattern a sparse grid of alignment markers by e-beam lithography onto the sample surface, followed by evaporation of 5 nm Ti and 50 nm Au and a lift-off process step.

We manufacture S-SWCNT array devices with two different layouts:

(1) Pd−S-SWCNT−Al junctions in which a built-in electric field across the S-SWCNT array is achieved by using two different contact metals.

(2) Pd−S-SWCNT−Pd devices with split top gates made of metal on top of a thin insulator.

In (1), we perform two e-beam lithography steps for defining the first and second contact metal followed by evaporation of 1 nm Ti/30 nm Pd/30 nm Au and 1 nm Ti/30 nm Al/30 nm Au, respectively. In (2), only one e-beam lithography step is necessary for patterning the contacts. In the next step, we coat all device sites with a local dielectric layer of 30 nm Al_2O_3 by atomic layer deposition through a PMMA mask defined by e-beam lithography. The Al_2O_3 layer serves two purposes. First, it is used as an etching mask to remove unwanted S-SWCNT material in an O_2-based plasma etching process step. Second, it serves as a gate dielectric for the split gate operation. The top gates made of 30 nm Ti are produced with varying spacing (0.25, 0.5, and 1 μm)

in a final e-beam lithography step. The spacing between the top gates determines the size of the intrinsic region in the p–i–n S-SWCNT array diode. The channel width is 10 μm for all S-SWCNT array devices investigated in this study.

Conflict of Interest: The authors declare no competing financial interest.

Acknowledgment. We thank Damon B. Farmer and Bruce A. Ek (IBM T. J. Watson Research Center) for expert technical assistance. M.C.H. acknowledges support by the National Science Foundation (DMR-1006391 and DMR-1121262) and the Nanoelectronics Research Initiative.

Supporting Information Available: This material is available free of charge via the Internet at http://pubs.acs.org.

REFERENCES AND NOTES

1. Avouris, P.; Freitag, M.; Perebeinos, V. Carbon-Nanotube Photonics and Optoelectronics. *Nat. Photonics* **2008**, *2*, 341–350.
2. Avouris, P. Carbon Nanotube Electronics and Photonics. *Phys Today* **2009**, *62*, 34–40.
3. Fujiwara, A.; Matsuoka, Y.; Suematsu, H.; Ogawa, N.; Miyano, K.; Kataura, H.; Maniwa, Y.; Suzuki, S.; Achiba, Y. Photoconductivity in Semiconducting Single-Walled Carbon Nanotubes. *Jpn. J. Appl. Phys. 2* **2001**, *40*, L1229–L1231.
4. Freitag, M.; Martin, Y.; Misewich, J.; Martel, R.; Avouris, P. Photoconductivity of Single Carbon Nanotubes. *Nano Lett* **2003**, *3*, 1067–1071.
5. Balasubramanian, K.; Fan, Y.; Burghard, M.; Kern, K.; Friedrich, M.; Wannek, U.; Mews, A. Photoelectronic Transport Imaging of Individual Semiconducting Carbon Nanotubes. *Appl. Phys. Lett.* **2004**, *84*, 2400–2402.
6. Misewich, J.; Martel, R.; Avouris, P.; Tsang, J.; Heinze, S.; Tersoff, J. Electrically Induced Optical Emission from a Carbon Nanotube FET. *Science* **2003**, *300*, 783–786.
7. Adam, E.; Aguirre, C. M.; Marty, L.; St-Antoine, B. C.; Meunier, F.; Desjardins, P.; Menard, D.; Martel, R. Electroluminescence from Single-Wall Carbon Nanotube Network Transistors. *Nano Lett.* **2008**, *8*, 2351–2355.
8. Wang, S.; Zeng, Q.; Yang, L.; Zhang, Z.; Wang, Z.; Pei, T.; Ding, L.; Liang, X.; Gao, M.; Li, Y.; *et al*. High-Performance Carbon Nanotube Light-Emitting Diodes with Asymmetric Contacts. *Nano Lett* **2011**, *11*, 23–29.
9. Pfeiffer, M. H. P.; Stürzl, N.; Marquardt, C. W.; Engel, M.; Dehm, S.; Hennrich, F.; Kappes, M. M.; Lemmer, U.; Krupke, R. Electroluminescence from Chirality-Sorted (9,7)-Semiconducting Carbon Nanotube Devices. *Opt. Express* **2011**, *19*, A1184–A1189.
10. Zhou, X.; Zifer, T.; Wong, B. M.; Krafcik, K. L.; Leonard, F.; Vance, A. L. Color Detection Using Chromophore-Nanotube Hybrid Devices. *Nano Lett.* **2009**, *9*, 1028–1033.
11. Rowell, M. W.; Topinka, M. A.; McGehee, M. D.; Prall, H.-J.; Dennler, G.; Sariciftci, N. S.; Hu, L.; Gruner, G. Organic Solar Cells with Carbon Nanotube Network Electrodes. *Appl. Phys. Lett.* **2006**, *88*, 233506.
12. Lee, J. U.; Gipp, P. P.; Heller, C. M. Carbon Nanotube P-N Junction Diodes. *Appl. Phys. Lett.* **2004**, *85*, 145.
13. Lee, J. U. Photovoltaic Effect in Ideal Carbon Nanotube Diodes. *Appl. Phys. Lett.* **2005**, *87*, 073101.
14. Yang, L.; Wang, S.; Zeng, Q.; Zhang, Z.; Pei, T.; Li, Y.; Peng, L.-M. Efficient Photovoltage Multiplication in Carbon Nanotubes. *Nat. Photonics* **2011**, *5*, 673–677.
15. Kang, S. J.; Kocabas, C.; Ozel, T.; Shim, M.; Pimparkar, N.; Alam, M. A.; Rotkin, S. V.; Rogers, J. A. High-Performance Electronics Using Dense, Perfectly Aligned Arrays of Single-Walled Carbon Nanotubes. *Nat. Nanotechnol.* **2007**, *2*, 230–236.
16. Engel, M.; Small, J. P.; Steiner, M.; Freitag, M.; Green, A. A.; Hersam, M. C.; Avouris, P. Thin Film Nanotube Transistors Based on Self-Assembled, Aligned, Semiconducting Carbon Nanotube Arrays. *ACS Nano* **2008**, *2*, 2445–2452.
17. Nemec, N.; Tomanek, D.; Cuniberti, G. Contact Dependence of Carrier Injection in Carbon Nanotubes: an Ab Initio Study. *Phys. Rev. Lett.* **2006**, *96*, 076802.
18. Leonard, F.; Talin, A. A. Electrical Contacts to One- and Two-Dimensional Nanomaterials. *Nat. Nanotechnol.* **2011**, *6*, 773–783.
19. Javey, A.; Guo, J.; Wang, Q.; Lundstrom, M. S.; Dai, H. Ballistic Carbon Nanotube Field-Effect Transistors. *Nature* **2003**, *424*, 654–657.
20. Zhang, Z.; Zhang, Z.; Liang, X.; Liang, X.; Wang, S.; Wang, S.; Yao, K.; Yao, K.; Hu, Y.; Hu, Y.; *et al*. Doping-Free Fabrication of Carbon Nanotube Based Ballistic CMOS Devices and Circuits. *Nano Lett.* **2007**, *7*, 3603–3607.
21. Freitag, M.; Tsang, J. C.; Bol, A. A.; Yuan, D.; Liu, J.; Avouris, P. Imaging of the Schottky Barriers and Charge Depletion in Carbon Nanotube Transistors. *Nano Lett.* **2007**, *7*, 2037–2042.
22. Wang, S.; Zhang, Z.; Ding, L.; Liang, X.; Shen, J.; Xu, H.; Chen, Q.; Cul, R.; Li, Y.; Peng, L.-M. A Doping-Free Carbon Nanotube CMOS Inverter-Based Bipolar Diode and Ambipolar Transistor. *Adv. Mater.* **2008**, *20*, 3258.
23. Chen, C.; Lu, Y.; Kong, E. S.; Zhang, Y.; Lee, S.-T. Nanowelded Carbon-Nanotube-Based Solar Microcells. *Small* **2008**, *4*, 1313–1318.
24. Gabor, N. M.; Zhong, Z.; Bosnick, K.; Park, J.; Mceuen, P. L. Extremely Efficient Multiple Electron-Hole Pair Generation in Carbon Nanotube Photodiodes. *Science* **2009**, *325*, 1367–1371.
25. Mueller, T.; Kinoshita, M.; Steiner, M.; Perebeinos, V.; Bol, A. A.; Farmer, D. B.; Avouris, P. Efficient Narrow-Band Light Emission From a Single Carbon Nanotube P-N Diode. *Nat. Nanotechnol.* **2010**, *5*, 27–31.
26. Kinoshita, M.; Steiner, M.; Engel, M.; Small, J. P.; Green, A. A.; Hersam, M. C.; Krupke, R.; Mendez, E. E.; Avouris, P. The Polarized Carbon Nanotube Thin Film LED. *Opt. Express* **2010**, *18*, 25738–25745.
27. Arnold, M. S.; Green, A. A.; Hulvat, J. F.; Stupp, S. I.; Hersam, M. C. Sorting Carbon Nanotubes by Electronic Structure Using Density Differentiation. *Nat. Nanotechnol.* **2006**, *1*, 60–65.
28. Hersam, M. C. Progress Towards Monodisperse Single-Walled Carbon Nanotubes. *Nat. Nanotechnol.* **2008**, *3*, 387–394.
29. Weisman, R. B.; Bachilo, S. M. Dependence of Optical Transition Energies on Structure for Single-Walled Carbon Nanotubes in Aqueous Suspension: an Empirical Kataura Plot. *Nano Lett.* **2003**, *3*, 1235–1238.
30. Luque, A.; Hegedus, S. *Handbook of Photovoltaic Science and Engineering*; John Wiley & Sons: New York, 2011.
31. Dattoli, E. N.; Wan, Q.; Guo, W.; Chen, Y.; Pan, X.; Lu, W. Fully Transparent Thin-Film Transistor Devices Based on SnO_2 Nanowires. *Nano Lett.* **2007**, *7*, 2463–2469.
32. Chen, Z.; Appenzeller, J.; Knoch, J.; Lin, Y.-M.; Avouris, P. The Role of Metal-Nanotube Contact in the Performance of Carbon Nanotube Field-Effect Transistors. *Nano Lett.* **2005**, *5*, 1497–1502.
33. Freitag, M.; Low, T.; Xia, F.; Avouris, P. Photoconductivity of Biased Graphene. *arXiv* 2012, cond-mat.mes-hall.
34. Xia, F.; Steiner, M.; Lin, Y.-M.; Avouris, P. A Microcavity-Controlled, Current-Driven, on-Chip Nanotube Emitter at Infrared Wavelengths. *Nat. Nanotechnol.* **2008**, *3*, 609–613.
35. Forrest, S. R. The Path to Ubiquitous and Low-Cost Organic Electronic Appliances on Plastic. *Nature* **2004**, *428*, 911–918.
36. Ahn, Y. H.; Dunning, J.; Park, J. Scanning Photocurrent Imaging and Electronic Band Studies in Silicon Nanowire Field Effect Transistors. *Nano Lett.* **2005**, *5*, 1367–1370.
37. Freitag, M.; Tsang, J. C.; Bol, A. A.; Avouris, P.; Yuan, D.; Liu, J. Scanning Photovoltage Microscopy of Potential Modulations in Carbon Nanotubes. *Appl. Phys. Lett.* **2007**, *91*, 031101.
38. Schroder, D. K. *Semiconductor Material and Device Characterization*; Wiley-IEEE Press, 2006; p 779.
39. Franklin, A. D.; Chen, Z. Length Scaling of Carbon Nanotube Transistors. *Nat. Nanotechnol.* **2010**, *5*, 858–862.
40. Xia, F.; Perebeinos, V.; Lin, Y.-M.; Wu, Y.; Avouris, P. The Origins and Limits of Metal-Graphene Junction Resistance. *Nat. Nanotechnol.* **2011**, *6*, 179–184.